Nanoscale

Accepted Manuscript

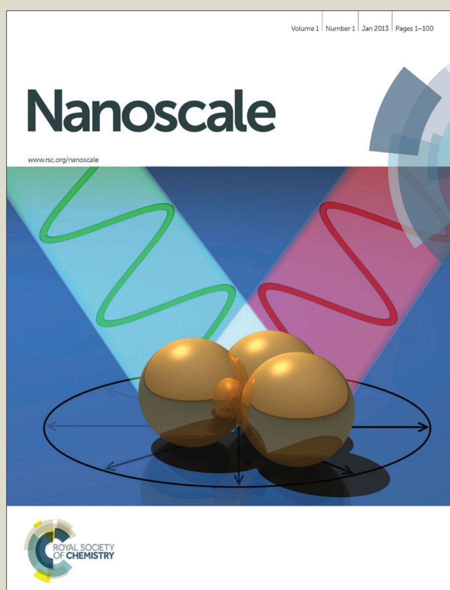

This is an *Accepted Manuscript*, which has been through the Royal Society of Chemistry peer review process and has been accepted for publication.

Accepted Manuscripts are published online shortly after acceptance, before technical editing, formatting and proof reading. Using this free service, authors can make their results available to the community, in citable form, before we publish the edited article. We will replace this *Accepted Manuscript* with the edited and formatted *Advance Article* as soon as it is available.

You can find more information about *Accepted Manuscripts* in the Information for Authors.

Please note that technical editing may introduce minor changes to the text and/or graphics, which may alter content. The journal's standard Terms & Conditions and the Ethical guidelines still apply. In no event shall the Royal Society of Chemistry be held responsible for any errors or omissions in this *Accepted Manuscript* or any consequences arising from the use of any information it contains.

ROYAL SOCIETY OF CHEMISTRY

www.rsc.org/nanoscale

Nanoscale RSCPublishing

Paper

Cite this: DOI: 10.1039/x0xx00000x

Characterization of nanometer-thick polycrystalline silicon with phonon-boundary scattering enhanced thermoelectric properties and its application in infrared sensors

Huchuan Zhou[1], Piotr Kropelnicki[2], and Chengkuo Lee[1]*

Received 00th July 2014,
Accepted 00th July 2014

DOI: 10.1039/x0xx00000x

www.rsc.org/

Although record-breaking low thermal conductivity of silicon nanowires has been reported, it remains as a challenge about integrating silicon nanowires with structure materials and electrodes in the CMOS process. In this paper, we investigated the thermal conductivity of nanometer-thick polycrystalline silicon (poly-Si) theoretically and experimentally. By leveraging the phonon-boundary scattering, the thermal conductivity of 52 nm thick poly-Si is as measured as low as around 12 W/mK which is only about 10% of the value of bulk single crystalline silicon. The ZT of n-doped and p-doped 52 nm thick poly-Si is measured as 0.067 and 0.024, respectively, while most of reported data are about 0.02 and 0.01 for poly-Si layer with thickness of 0.5 μm and above. Thermopile infrared sensors comprising 128 pairs of thermocouple made of either n-doped or p-doped nanometer-thick poly-Si strips in series connection with aluminium (Al) metal interconnect layer are fabricated using microelectromechanical system (MEMS) technology. The measured vacuum specific detectivity (D*) of n-doped and p-doped thermopile infrared (IR) sensors are $3.00*10^8$ and $1.83*10^8$ $cm*Hz^{1/2}*W^{-1}$ for sensors of 52nm thick poly-Si, and $5.75*10^7$ and $3.95*10^7$ $cm*Hz1/2*W^{-1}$ for sensors of 300nm thick poly-Si, respectively. The outstanding thermoelectric properties indicate our approach promising in diversified applications using ultrathin poly-Si technology.

Nowadays, thermoelectric microdevices using Seebeck effect, i.e., self-generated voltage due to the temperature difference created between two ends of thermocouple-like structures, are commercialized and demonstrated as the diversified applications including non-contact temperature sensing [1], infrared (IR) focal plane array (FPA) [2-5], air flow sensors [6], gas sensors [7], accelerometers [8,9] and AC-DC converters [10]. On the other hand, Peltier effect has been deployed in thermoelectric microdevices for thermoelectric cooler application [11-17]. With the aid of microelectromechanical system (MEMS) technology, various configurations of thermoelectric microdevices are realized on silicon substrates and polymer-based flexible substrates, for examples, suspended thermoelectric membranes are created on micro-cavities [18-20] or vertical thermocouple array is formed in polymer substrates [21-22]. Array of thermocouple connected in series, so-called thermopile, is normally implemented in order to boost up the output voltage.

The most widely used thermoelectric materials are the Tellurium (Te) alloy with Bismuths (Bi), Antimony (Sb), and so on [23-31], which have high figure-of-merit, $ZT=\alpha 2T/\rho k\approx 1$, where α, ρ, k and T are the Seebeck coefficient, electrical resistivity, thermal conductivity and absolute temperature, respectively. It remains as a challenging task of having thermoelectric materials with $ZT > 1$ within wide operation temperate range [32]. CMOS materials such as Silicon (Si) and Silicon-Germanium (SiGe) have been characterized as promising thermoelectric materials. However, relatively high thermal conductivity of Si (~150 $Wm^{-1}K^{-1}$) at room temperature makes the ZT of Si low at room temperature. Recently a few studies report significant enhancement in ZT of nanostructured Si to reduce the thermal conductivity by enhancing phonon scattering [33-37]. The great increment of phonon-boundary scattering leads drastic reduction in thermal conductivity when the characteristic length scales are smaller than the mean free path of phonon at nanometer scale [33]. For bulk silicon, the mean free path of phonon is around 300 nm at room temperature [34]. Si nanowires, for instance, have been reported possessing thermal conductivity as low as 0.73 $Wm^{-1}K^{-1}$, which enhances ZT for more than 100 times with respect to the typical bulk value [35]. Meanwhile, using Si phononic nanomesh structures, the thermal conductivity of close to 1.5 $Wm^{-1}K^{-1}$ is

[1]*Electrical and Computer Engineering, National University of Singapore, 4 Engineering Drive 3, 117576, Singapore. E-mail: elelc@nus.edu.sg.*
[2]*Excelitas Technologies, 8 Tractor Rd., 627969, Singapore.*

Nanoscale Accepted Manuscript

reported [36, 37]. However, it is a great challenge in the fabrication process from the mass production aspect when we want to incorporate Si nanowires or Si nanomesh in a planar thermopile structure which is the mainstream configuration so far. Besides, the thermoelectric characteristics of Si nanowires highly depend not only on their dimension but also on the nanoscopic surface morphology [38-40]. Thus top-down fabrication technology can leverage reliable and predictable material properties of single crystal Si and polycrystalline Si (poly-Si). The thermal conductivity of single crystal Si with thickness of about 100nm has been studied [34, 41], showing an over 50% reduction to thermal conductivity to around 50Wm^{-1}K^{-1}. However, this value is still much larger than the thermal conductivity of bulk poly-Si, which is around 30 Wm^{-1}K^{-1}[42, 43], because the grain boundary scatter phonons leading to reduction in thermal conductivity [44]. Besides, a portion of n-doped dopants segregate to the grain boundaries in poly-Si, also contributing to greater phonon scattering [45]. The advanced CMOS manufacturing technology can allow features of a few tens nanometers and thin poly-Si layers of a few nanometers fabricated in 12" wafer. In view of the strong needs of high *ZT* CMOS thermoelectric materials, we investigate ultrathin poly-Si in order to enhance the *ZT* based on phonon-boundary scattering. Subsequently, a scalable design of thermopile is fabricated in a CMOS mass production line based on ultrathin polycrystalline Si with optimized *ZT* and device configurations.

To investigate how thickness of thin poly-Si layer affect on the *ZT*, micromachined test-keys are deployed to study the thermal conductivity, Seebeck coefficient and electrical resistivity of n/p-doped poly-Si layer. The test-key is shown in **Fig. 1** and the testing setup is the same as the one reported in authors' previous work [5].

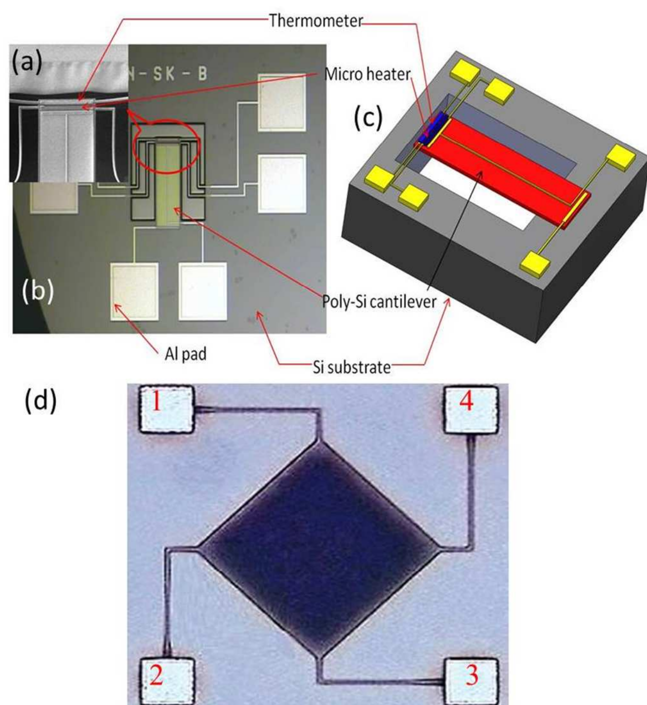

Fig. 1 SEM image (a), optical microscope image (b) schematic drawing (c) of test-key of thermal conductivity; and optical image of the test-key of electrical resistivity (d).

The Seebeck coefficient and thermal conductance were determined by a cantilever test structure as shown in **Fig. 1 (a), (b) and (c)**, which performs as a single thermocouple using poly-Si and aluminium (Al) as the thermocouple pair materials. The cantilever comprises of three layers: thermal SiO_2, doped poly-Si and PECVD SiO_2, while the narrow Al line connects the hot-junction and cold-junction for electrical signal readout. The geometries of the n-type and p-type cantilever test structures are the same. The thickness of poly-Si in the test structure is 52 nm, 73 nm, 102nm 123nm and 300nm, while the width is 90 µm and the length is 300 µm. The width and the thickness of the Al line are 1 µm and 100nm. A micro-heater is arranged at the suspended end to heat up the hot-junction of the test structure while the other end connects to Si substrate which is kept at ambient temperature, (T_0) as a cold junction. A thermometer made by poly-Si is arranged at the end of the hot-junction to monitor the temperature, T_1, by monitoring the resistance of the thermometer. The thermal conductance, K_c, and Seebeck coefficient, α_{Si}, can be calculated with **Equation 1 and 2**:

$$K_c = \frac{{V_{in}}^2}{R_{heater}}(T_1 - T_0)^{-1} \quad , \quad (1)$$

$$\alpha_{Si} = \frac{V_{out}}{T_1 - T_0} + \alpha_{Al} \quad , \quad (2)$$

where V_{in} is the voltage applied on the micro heater, R_{heater}, is the electrical resistance of the heater; V_{out} is the output voltage and α_{Al} is the Seebeck coefficient of Al. The magnitude of Seebeck coefficient of Al is less than 2 so the Al wire will not affect the measured Seebeck coefficient of Poly-Si significantly. The thermal conductivity, on the other hand, will be affected by the Al wire and SiO_2 layer since the contribution to overall thermal conductance of the cantilever from Al and SiO_2 is not negligible. Because the thickness and width of Al and SiO_2 are the same for all test-keys and the only difference is the thickness of poly-Si and so it is possible to eliminate the influence of Al and SiO_2.

A van-der-Pauw structure as shown in **Fig. 1 (d)** was used to study the electrical resistivity of the heavily doped poly-Si. The average electrical resistivity of a sample is given by

$$\rho = R_s * t, \quad (3)$$

where R_s is the sheet resistance and t is the thickness of the poly-Si. To conduct the measurement, we apply a current to flow along one edge of the sample, for instance, I_{12}, where the pad number mark is indicated in Fig. 1(d), and measure the voltage across the opposite edge, i.e., V_{34} in this case, to calculate a resistance, i.e., $R_{12,34}$, using Ohm's law:

$$R_{12,34} = V_{34}/I_{12} \quad (4)$$

With the same method, $R_{23,41}$ can also be measured. Then the sheet resistance R_s can be defined as follows [53]:

$$e^{-\pi R_{12,34}/R_s} + e^{-\pi R_{23,41}/R_s} = 1 \quad (5)$$

Then the temperature coefficients of resistance (TCRs) of the poly-Si are measured by varying the temperature with a temperature stabilizer and further study of the I/V curve. TCR describes the temperature dependence of resistance as $R(T) = R(T_0) * (1 + TCR * (T - T_0))$, where R(T) is the resistance at temperature T while $R(T_0)$ is the resistance at the original temperature T_0. The measured TCR is -0.20%K^{-1} and -0.15%K^{-1} for n-doped poly-Si and p-doped poly-Si, respectively. The measured thermal conductivities of n/p-doped poly-Si with different thickness at room temperature are shown **Fig. 2 (a).** The results show that the thermal conductivity decreases when the poly-Si thickness reduces.

This phenomenon becomes more significantly when the thickness is less than 150 nm. By using frequency-dependent relaxation time to demonstrate the effects of phonon scattering events, Callaway

Nanoscale Accepted Manuscript

This journal is © The Royal Society of Chemistry 2012

reported a theoretical model with one approximate solution to the Boltzmann transport equation for phonons in 1959 [41]. Later in 1963, Holland improved this method by taking phonon polarization into account [42]. Furthermore, A. D. McConnell and her colleagues expanded this model by adding in the study on the effect of grain boundaries and the dopant impurities [43].

Both mobile carriers and phonons contribute to the overall thermal conductivity of poly-Si as shown in **Equation 6**:

$$k = k_e + k_p \quad , \qquad (6)$$

where $\boldsymbol{k_e}$ is the thermal conductivity induced by electrons and $\boldsymbol{k_p}$ is the thermal conductivity induced by phonons. According to Wiedemann–Franz law, $\boldsymbol{k_e}$ at certain temperature, T, can be defined by **Equation 2** below:

$$k_e = \frac{\pi^2 K_B^2 T}{3q^2\rho} \quad , \qquad (7)$$

where K_B is the Boltzmann constant, q is the electron charge and $\boldsymbol{\rho}$ is the electric resistivity of poly-Si. Since the electric resistivity of doped poly-Si is in the magnitude of 10^{-5} Ωm [44], the estimated value of $\boldsymbol{k_e}$ is less than 1 $Wm^{-1}K^{-1}$ which is not significant compared to the overall thermal conductivity. Therefore, it is reasonable to claim that the phonon scattering events dominate.

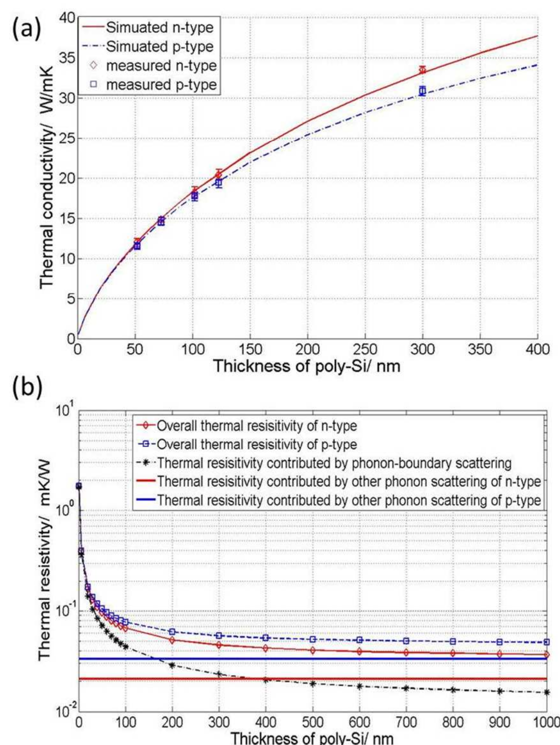

Fig.2 Measured and simulated thermal conductivity of ultrathin poly-Si (a); and thermal resistivity of poly-Si influenced by different kinds of phonon scattering (b) versus poly-Si thickness.

Using Callaway and Holland's model, thermal conductivity induced by phonons, $\boldsymbol{k_p}$, can be calculated with **Equation 8** below:

$$k_p = \frac{1}{3}\left(\frac{k_B T}{h/2\pi}\right)^3 \frac{k_B}{2\pi^2}\sum_{j=L,TO,TU}\frac{1}{v_j}\int_0^{\theta_j/T}\frac{x_\omega^4 e^{x_\omega}\tau_j}{(e^{x_\omega}-1)^2}dx_\omega \qquad (8)$$

where x_ω is dimensionless phonon angular frequency which is defined as $x_\omega = h\omega/2\pi K_B T$, h is Planck's constant, k_B is Boltzmann constant, T is the temperature and τ_j is the phonon relaxation time. This method presents the phonon scattering events in longitudinal model and transverse model, while the transverse model is divided into low-frequency model and high-frequency model. The symbol *L*, *TO* and *TU* in **Equation 8** refer to the longitudinal model, low-frequency transverse model and high-frequency transverse model, respectively. The v_j is the phonon group velocity in different modes. In silicon, v_L=*8.84*10*^{3} *m/s*, v_{TO}=*5.86*10*^{3} *m/s* and v_U=*2.0*10*^{3} *m/s*.

The relaxation time τ_j for each model cantains servral phonon scattering events as shown in **Equation 9**:

$$\tau_j^{-1} = \sum_i \tau_{j,i}^{-1}. \qquad (9)$$

Generally, there are phonon-phonon scattering, phonon-electron scattering, phonon-boundary scattering and mass-difference impurity scattering [43]. In comparison to the other three factors, phonon-electron scattering is negligible [45]. Furthermore, phonon scattering on grain boundary and segregated dopants also contributes to the relation time in the case of doped poly-Si. Since the thickness we chose is much less than the mean free path of phonon (~300 nm at room temperature), the phonon-boundary scattering should be the key in this study. The detail description of other phonon scattering events has been discussed by Holland[42]. We emphasize on the influence of phonon-boundary scattering. First of all, the phonon relaxation time induced by phonon-boundary scattering is shown in **Equation 10**:

$$\tau_{boundary}^{-1} = \frac{v_s}{d}\left(\frac{1-p}{1+p}\right) \qquad (10)$$

where d is the thickness of poly-Si, $\boldsymbol{v_s}$ is an averaged phonon group velocity which can be defined as $v_s^{-1} = (2/v_{TO} + 1/v_L)/3$. And p is a parameter with value between 1 and 0, representing the surface roughness parameter which is the probability of specula reflection from the sample boundary. $p=1$ means a perfectly smooth surface reflecting all incoming phonons while $p=0$, on the other hand, represents an entirely rough surface that diffusely scatters all incident phonons like a blackbody.

With the above-mentioned equations, we conducted the simulation to derive thermal conductivity of poly-Si using Matlab 2010b. The simulation results of thermal conductivity of both n/p-doped poly-Si with different thickness are also shown Fig. 2(a). The thermal conductivity of both n/p-doped poly-Si decreases as the thickness of the poly-Si layer reduces. It matches with the measured data well. Noticing from Equation 5, the phonon relaxation time induced by the phonon-boundary scattering event is inversely proportional to the thickness of poly-Si.

In order to understand how the phonon-boundary scattering affect the overall thermal conductivity, an simulation of the contribution of phonon-boundary scattering to the overall thermal conductivity compared to other phonon scattering events as been conducted. **Fig. 2(b)** shows the contribution of phonon-boundary scattering to the overall thermal conductivity compared to other phonon scattering events. It is clearly observed that the thermal resistivity is dominated by the phonon-boundary scattering when the thickness of poly-Si layer is less than 100 nm, while the other phonon scattering events are not affected by the change of poly-Si layer thickness.

Moreover, the electrical resistivity and Seebeck coefficient of poly-Si layer with different thickness are also measured and shown in **Fig. 3 (a) and (b).** It suggests that these two parameters are intrinsic

Nanoscale Accepted Manuscript

properties which are subject to doping concentration and do not change with the poly-Si thickness. According to the calculated Figure of merit, *ZT*, (**Fig. 3(c)**), the n-doped poly-Si has much higher *ZT* compared to p-doped poly-Si among measured data of all 5-kinds of thickness variation in this experiment. This is because n-doped poly-Si has relatively lower electrical resistivity and higher Seebeck coefficient compared to p-doped poly-Si. Besides, the trend of the change of *ZT* along with poly-Si thickness variation reflects the trend of thermal conductivity change regarding poly-Si thickness shown in **Fig. 3(a).** It is observed that the maximum *ZT* of 0.067 and 0.024 are obtained for the 52 nm thick n/p-doped poly-Si layer, respectively. Such results show a 116% and 92% increment in *ZT* when the thickness of poly-Si layer decrease from 300 nm to 52 nm. Generally speaking, *ZT* of bulk poly-Si is around 0.01 because of the relatively high thermal conductivity (~30Wm^{-1}K^{-1}) [20, 51].

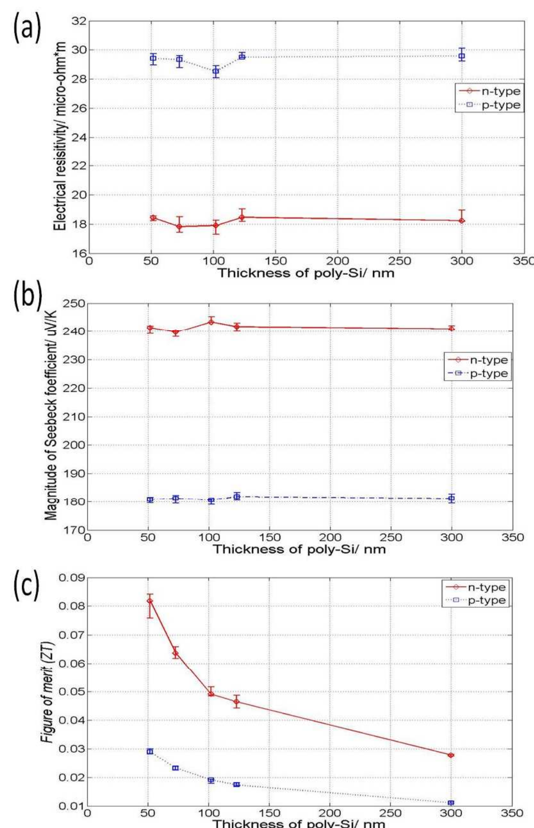

Fig.3 The electrical resistivity (a), Seebeck coefficient (b) and figure of merit, ZT, (c) measured at room temperature.

Table 1. The comparison of the thermoelectric properties measured in this work to other states of art.

Poly-Si type	**Thermal conductivity (W/mK)**	Seebeck coefficient (μV/K)	Electrical resistivity (μΩm)	Figure of merit ZT	Details
n-type	**12.1**	-242.1	18.3	0.067	This work: t=52nm, heavily doped
	31.5	-57	8.1	0.004	Bulk, t>1μm, intrinsic[51]
	29.7	-110	8.9	0.014	Bulk, t~700nm, heavily doped [20]
p-type	**12.0**	182.3	28.9	0.024	This work: t=52nm, heavily doped
	31.2	103	22.1	0.005	Bulk, t>1μm, intrinsic[51]
	28.4	130	13.7	0.012	Bulk, t~700nm, heavily doped [20]

The comparison of the thermoelectric properties measured in this work to other states of art has been shown in **Table 1**. From the above discussion of ultrathin poly-Si thermoelectric data, the thermopile using ultrathin poly-Si layer are developed and characterized in this session. **Fig. 4** shows the schematic drawing of a thermopile which possesses a cross-like suspended membrane structure with IR absorber coated at the center square area. When the thermopile is exposed to IR radiation, the central absorber area absorbs the radiation and turns the radiation power into heat. Such received radiation heat causes a temperature rise at the central part of the thermopile, i.e., it is defined as hot-junction of thermocouples. The other end of the thermocouples in the thermopile connecting with the single crystalline Si substrate is maintained at room temperature during the measurement because of the high thermal conductance and large thermal mass of the Si substrate. As a result, there is a temperature difference between the hot-junction and cold-junction which brings a self-generated voltage between two ends of the thermopile, i.e., the hot-junction and cold-junction.

The thermopile comprises 128 pairs of series connected thermocouple and the schematic drawing of one single thermocouple is shown in Fig. 4. The doped poly-Si strips are built at the bottom as the one material of the thermocouple while Al is another material which also forms an electrical connection between each thermocouple. According to Seebeck effect, the temperature difference between the two ends of the thermocouples will induce a voltage drop which can be read out through the contact pads.

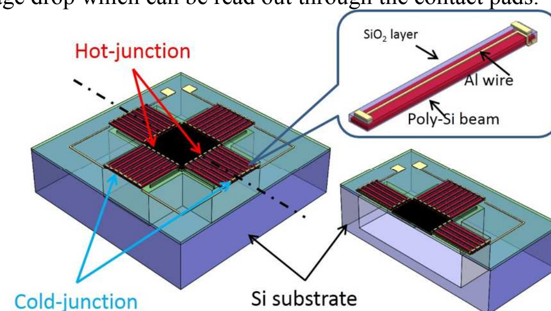

Fig.4 Schematic drawing of the IR sensor and single thermocouple.(not to scale)

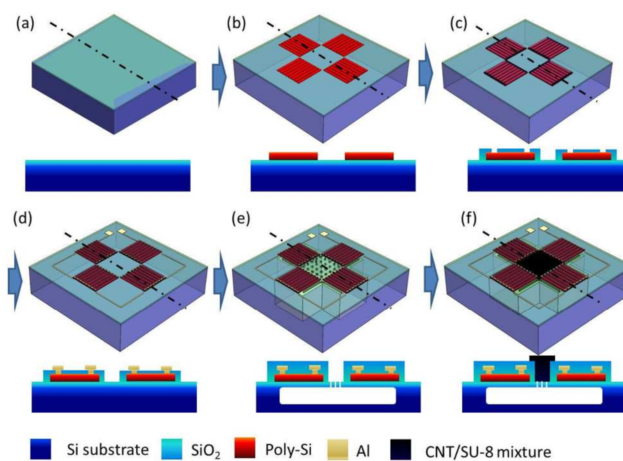

Fig.5 Process flow of the device. Wafer start with Si substrate and thermal SiO2 on top (a); poly-Si strip deposition, doping and pattering (b); SiO2 electric isolation layer deposition, contact via open and implantation (c); Al wire deposition and patterning (d); SiO2 passivation layer deposition, contact pad open and structure release (e); CNT/SU-8 IR absorber deposition (f).

Nanoscale Accepted Manuscript

This journal is © The Royal Society of Chemistry 2012

The thermopile structure is fabricated with all CMOS process. **Fig. 5** illustrates all the fabrication process flow of the ultrathin poly-Si based thermopile IR sensor. The process started with an 8-inch bare Si wafer with 40nm thermal SiO_2 on top (**Fig. 5 (a)**). Then poly-Si with different thickness are deposited at 760°C and doped as n-type and p-type with different wafers. The thickness variation of poly-Si is the same as the test-key presented in previous text. After that the poly-Si are patterned with photo-lithography and plasma etching (**Fig. 5 (b)**). Subsequently a 30nm thick SiO_2 was built as an electrical isolation layer with plasma enhanced chemical vapor deposition (PECVD) process; then the contact via was open on SiO_2 and an additional surface heavy implantation was conducted to reduce the electrical contact resistivity between the poly-Si and Al; after the contact implantation the whole wafer is annealed with N_2 circumstance at 1050°C for 30 minutes (**Fig. 5 (c)**). After the annealing Al was deposited and patterned following with annealing in N_2 circumstance at 420°C for 30 minutes to achieve better electrical connection (**Fig. 5 (d)**). Subsequently another 30 nm PECVD SiO_2 passivation layer was deposited and then open contact area for Al pad; after that release slots and holes were opened and the whole structure was released using XeF_2 (**Fig. 5 (e)**). After releasing the structure, a drop of solution comprising carbon nanotube (CNT) mixed with SU-8 was deposited at the central part of the thermopile as a broadband IR absorber (**Fig. 5 (f)**).

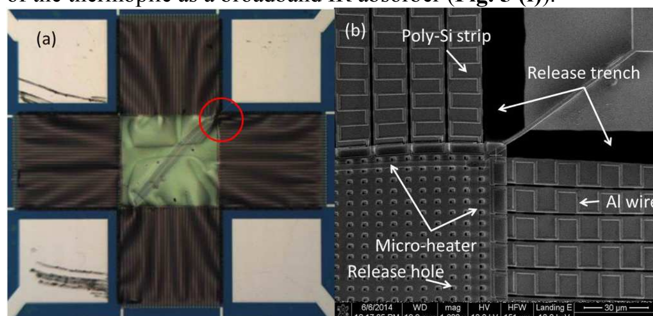

Fig.6 Optical microscope image of the thermopile structure without absorber coating (a); SEM image of the zoom-in view (b).

A fabricated device is shown in Fig. 6. The blur parts in **Fig. 6 (a)** are due to the stress induced by SiO2 and poly-Si layers. This stress can be reduced by using Al_2O_3 as a dielectric layer instead of SiO_2. However, Al_2O_3 possesses much higher thermal conductivity compared to SiO_2, which will draw back the performance of the thermopile. Even though the stress, induced by SiO2 in Fig. 6(a), seems large but the SiO_2 membrane can provide enough mechanical strength to this structure [49]. That is the reason authors choose SiO_2 as dielectric layer to build the thermopile. The Scanning electron microscope (SEM) image and the Fourier transform infrared spectroscopy (FTIR) characterization of the CNT/SU-8 mixture absorber are shown in **Fig. 7(a)**. As shown in this figure, the surface of the CNT/SU-8 mixture absorber is not smooth. It is due to the imperfect of manual process of coating the absorber onto the IR thermopile. The absorption of IR radiation is very high up to over 98.5% from 2μm to 8μm.

In order to characterize the performance of the thermopile IR sensor using ultrathin poly-Si, an electrical measurement is conducted using a micro-heater placed at the central part of the thermopile to mimic the IR radiation as shown in **Fig. 6(b).** According to our previous work [49], usage of micro-heater to simulate the IR radiation only introduces 1% difference.

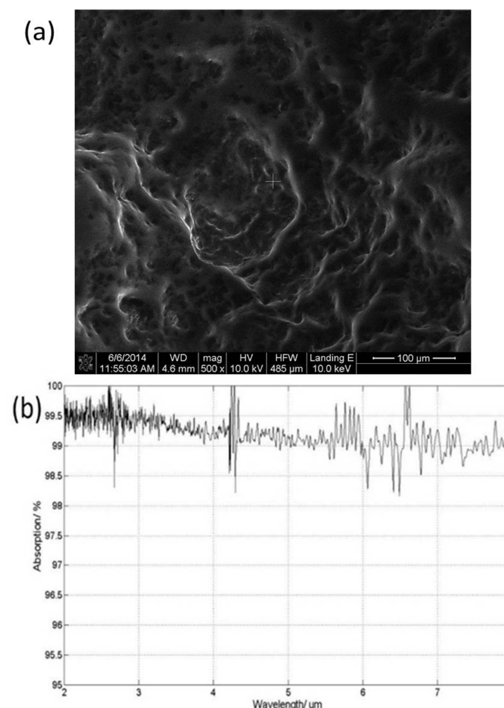

Fig.7 The Scanning electron microscope (SEM) image (a) and the Fourier transform infrared spectroscopy (FTIR) measurement results (b) of the CNT/SU-8 mixture absorber.

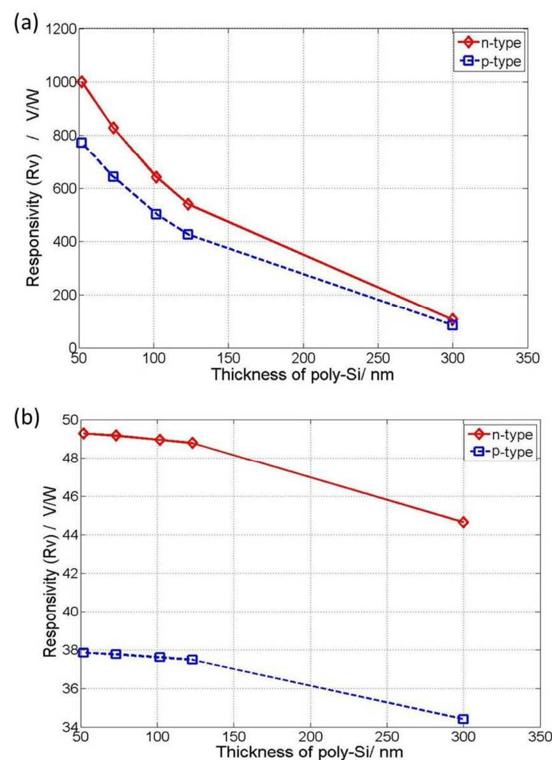

Fig.8 Electrical testing measured responsivity (Rv) of n/type poly-Si with vacuum (a) and at atmospheric pressure (b).

Nanoscale Accepted Manuscript

The efficiency of a thermopile is usually evaluated by two parameters: the responsivity, R_v, and the specific detectivity, D^*. R_v presents the efficiency of converting heat to electricity, while D^* stands for how precise the sensor can detect [20]. The definition of R_v and D^* are shown as follows:

$$R_v = \frac{V_{out}}{P_{in}}\ , \tag{11}$$

$$D^* = R_v\sqrt{A\Delta f}/V_n, \tag{12}$$

where V_{out} is the output voltage and P_{in} is the infrared power applied to the thermopile; A is the IR absorption of the integrated absorber; Δf is the frequency bandwidth of the read out system, V_n is the noise equivalent voltage.

The electrical testing was conducted at room temperature and the testing results of n-doped and p-doped poly-Si based thermopile are shown in **Fig. 8**. The results of the experiment conducted in vacuum are shown in **Fig. 8 (a)**, the thermopile with the thinnest (52nm) poly-Si layer, no matter n-doped or p-doped, possesses the highest R_v. The R_v of thermopile with 52 nm-thick n-doped poly-Si is 1000.1 VW^{-1} while the R_v of thermopile with 300 nm-thick n-doped poly-Si is 105.8 VW^{-1}, which indicates 845% improvement by reducing poly-Si thickness. Similarly, the thermopile using p-doped poly-Si also shows a great improvement with respect to thinner poly-Si. R_v is 772.5VW^{-1} and 84.4VW^{-1} for the p-doped thermopile with 52nm-thick poly-Si and 300nm-thick poly-Si, where 815% improvement is observed for the thinner p-doped poly-Si.

In order to study the influence of air on the performance of thermopile, authors conducted the measurement again at atmospheric pressure and results are shown in **Fig. 8 (b)**. In contrast to the measurement results in vacuum, the R_v of all thermopiles decrease over an order of magnitude. Besides, the enhancement of R_v, caused by reduction of poly-Si thickness, is not so significant compared to the results achieved in vacuum. This is because the thermal conductivity of air dominates when the thermopile is working at atmospheric pressure. R_v of n-doped and p-doped poly-Si with thickness of 52nm decrease to 24.8 VW^{-1} and 19.0 VW^{-1}, respectively. Compared to the R_v achieved in vacuum test the reduction is over 97%. On the other hand, R_v of n-doped and p-doped poly-Si with thickness of 300nm do not show such great decreasing, which is 23.6 VW^{-1} and 18.1 VW^{-1}, respectively, with the reduction of only about 78% compared to the case in vacuum. Since the thermal conductance from air is the same for all thermopiles, due to the same surface area, the reduction in thermal conductance of the structure is not so significant to the overall thermal conductance.

Table 2 Calculated time constant of the thermopile IR sensors

Thickness of poly-Si (*nm*)		52	73	102	123	300
Time constant in vacuum (*ms*)	n-doped	87	77	65	58	30
	p-doped	87	78	66	60	32
Time constant at atmospheric pressure (*ms*)	n-doped	0.85	0.89	0.94	0.98	1.27
	p-doped	0.85	0.89	0.94	0.98	1.27

After the characterization of the thermopile structure, authors conducted an IR radiation test using a blackbody with temperature of 470°C as IR radiation source. According to the Planck's curve, the radiation peak is around 3.9 µm, which is in the absorption range of the CNT/SU-8 mixture absorber. The details of testing setup of the radiation test have been reported in our previous work [5].

The IR radiation test was conducted in vacuum and only at room temperature. The results are shown in **Fig. 9(a) and (b)**. It is clear that the thermopile IR sensor using 52nm-thick poly-Si has the highest output. For n-doped and p-doped microdevice the value is approximate 890% and 700% compared to that of the thermopile IR sensor using 300nm-thick poly-Si, respectively. As shown in Fig. 9 (a) and (b), the output voltage decreases with higher chopper frequency because the thermopile needs time to be heated up. The thermal time constant of the thermopile IR sensor can be decided by the time required to reach 63% of the maximum detector output voltage [52]. Using the data shown in Fig. 9 (a) and (b) the calculated time constant of the thermopile IR sensors with different poly-Si thicknesses and doping types are shown in **Table 2**.

Since the absorption of the IR absorber is not 100%, the responsivity, R_v, of the IR sensor is different from the R_v measured by the electrical testing. By using the Planck's equation, authors estimate the power applied on the IR sensor is 29.7 µW. Then the R_v of the IR sensor is derived with the estimated radiation power and the output voltage are shown in **Fig. 10 (a).**

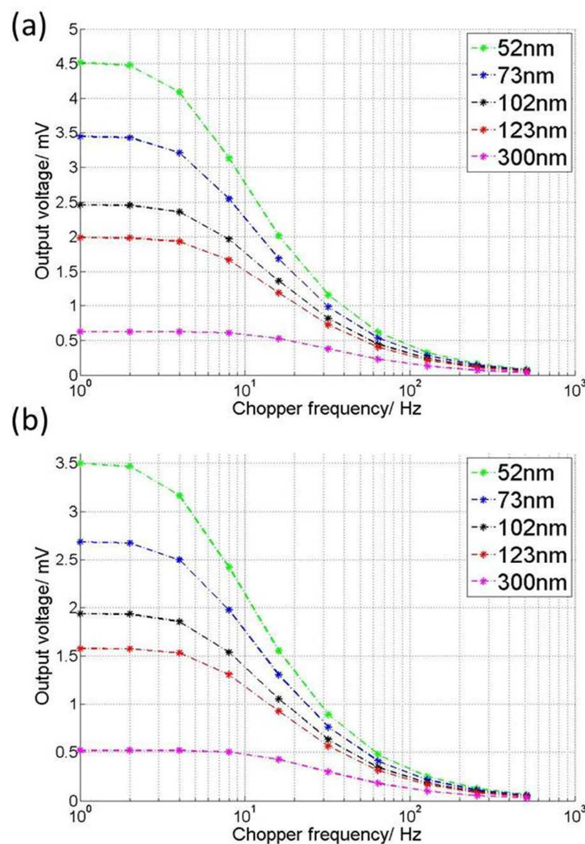

Fig.9 IR response of n-doped poly-Si (a) and p-doped poly-Si (b) thermopile with different chopper frequency.

Nanoscale Accepted Manuscript

 This journal is © The Royal Society of Chemistry 2012

According to the data shown in this figure, the R_v of the IR sensor is only slightly smaller than the perfect R_v from the electrical test. The overall emissivity, ε, of the IR sensor is further calculated using **Equation 13**

$$\varepsilon = \frac{R_{v_IR}}{R_{v_electrical}} \quad (13)$$

where R_{v_IR} is the R_v of the IR sensor and $R_{v_electrical}$ is the perfect R_v get from the electrical test. The average overall emissivity is calculated as 95%.

The overall series electrical resistances of all the sensors are also measured and the results are shown in **Table 3**. Since there is no current flow through the microdevice, there is no *1/f* noise but only Johnson noise of the thermopile IR. The Johnson noises are estimated with the measured series electrical resistances and shown in **Table 3**. Then the specific detectivity, D^*, of each thermopile IR sensor is further estimated as shown in **Fig. 10 (b).** The thermopile IR sensors with thinner poly-Si possess the higher D^*, which is the same as the testing results of R_v. The D^* of n-doped poly-Si with thickness of 52nm and 300nm are $3.00*10^8$ and $5.75*10^7$ $cm*Hz^{1/2}*W^{-1}$, respectively, while the D^* of p-doped poly-Si with thickness of 52nm and 300nm are $1.83*10^8$ and $3.95*10^7$ $cm*Hz^{1/2}*W^{-1}$, respectively. As shown above, the enhancement in D^* of n-doped and p-doped thermopile with ultrathin poly-Si is 421% and 364%, respectively. However, compared with the stated value of R_v, we do not see such significant enhancement in D^*, because of higher noise induced by increase of electrical resistance of thinner poly-Si strip.

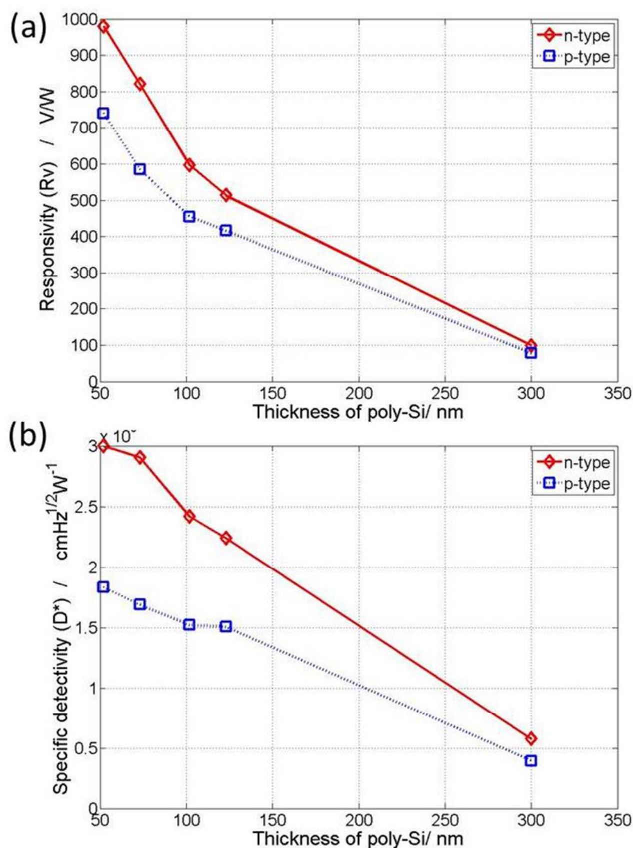

Fig.10 Measured responsivity (a) and specific detectivity D* (b) in vacuum.

Table 3 Measured series electrical resistance and estimated Johnson noise of the thermopile IR sensors

Thickness of poly-Si (nm)		52	73	102	123	300
Series electrical resistance ($10^6\Omega$)	n-doped	1.91	1.43	1.09	0.94	0.52
	p-doped	2.91	2.14	1.60	1.37	0.70
Estimated Johnson noise ($\mu VHz^{-1/2}$)	n-doped	0.18	0.15	0.13	0.12	0.09
	p-doped	0.22	0.19	0.16	0.15	0.11

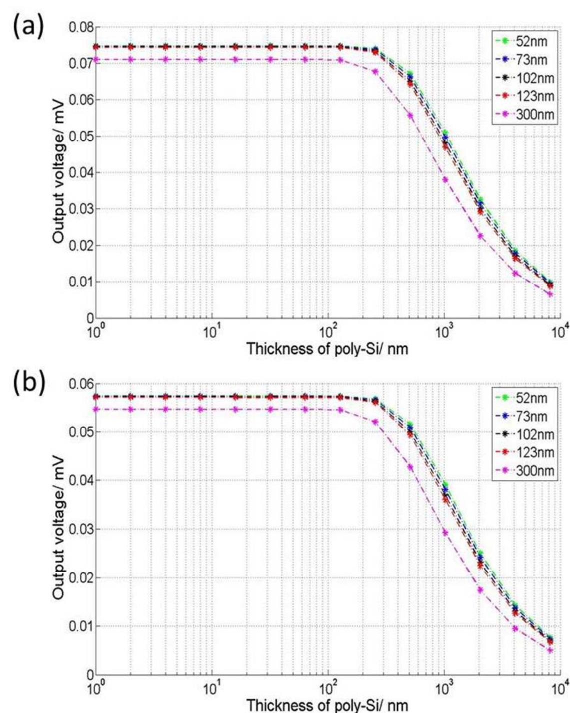

Fig.11 IR response of n-doped poly-Si (a) and p-doped poly-Si (b) thermopile with different chopper frequency.

The radiation test was also conducted at atmospheric pressure and the results are shown in **Fig. 11** and **Fig. 12.** As shown in Fig. 11 (a) and (b), the response of the sensor becomes much faster due to the large thermal conductance caused by air. The calculated time constant of the IR sensor is shown in **Table 2** as well. The main difference of the IR test results at atmospheric pressure, compared to the data measured in vacuum, is that D^* increases along with the thickness of poly-Si. As discussed above, since it is the thermal conductance of air dominates in this case, the reduction of overall thermal conductivity caused by the decreasing poly-Si thickness is not as significant as in vacuum. Therefore, the enhancement of R_v is also not so significant. The noise, on the other hand, increases by reducing the thickness of poly-Si. That is the reason why the D^*, shown in **Fig. 12(b)**, shows different trend when the sensor working at atmospheric pressure.

By leveraging the straightforward fabrication approach, the sound thermoelectric properties of ultrathin poly-Si have been obtained because of phonon-boundary scattering effect. This fabrication process is fully CMOS compatible without using other advanced

Nanoscale Accepted Manuscript

nanofabrication technologies, e.g., electron beam lithography (EBL), etc. The demonstrated R_v and D^* of thermopile IR sensor are promising for various applications.

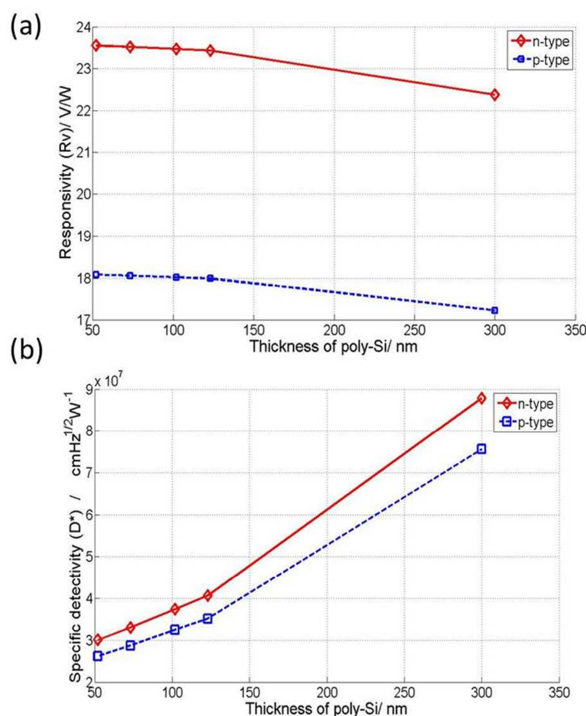

Fig.12 Measured responsivity (a) and specific detectivity D* (b) at atmospheric pressure.

Conclusion

In this paper, authors studied the thermoelectric properties of ultrathin poly-Si, showing an impressive enhancement in *ZT* by decreasing the thickness of poly-Si to reduce thermal conductivity, due to stronger phonon-boundary scattering. The maximum *ZT* of 0.067 and 0.024 are obtained for the 52 nm thick n-and p-doped poly-Si layer, respectively. Such results show a 116% and 92% increment in *ZT* when the thickness of poly-Si layer decreases from 300 nm to 52 nm. Then, the design, fabrication and testing of the thermopile IR sensor, using ultrathin poly-Si, is presented to demonstrate its applications for thermoelectric devices. The measured R_v of the IR senor using 52 nm n- and p-doped poly-Si is 1000.1 VW^{-1} and 772.5VW^{-1} in vacuum, respectively. D^* of the IR senor using 52 nm n- and p-doped poly-Si is $3.00*10^8$ and $1.83*10^8$ $cm*Hz^{1/2}*W^{-1}$, respectively. This result illustrates that the R_v of thermopile IR sensor using 52nm poly-Si is improved over 845% and 815% compared to the sensor using 300nm poly-Si for n-doped and p-doped in vacuum, respectively. While the D^* of thermopile IR sensor using 52nm poly-Si is improved 421% and 364% in vacuum compared to the sensor using 300nm poly-Si for n-doped and p-doped. This result indicates the advantage of the poly-Si with thickness in nanometer scale as a promising thermoelectric material.

Acknowledgements

The authors acknowledge the financial support from research grants of, SinBerBEST (WBS: R-263-000-A34-592) "TinyCO2 project: Enabling CO2 Sensing at the Millimeter Scale and Ultra-Low Cost for Distributed HVAC Sensing/Control" and AcRF Tier 2 - MOE2012-T2-2-154 (WBS: R-263-000-A59-112) at the National University of Singapore, and the National Research Foundation (NRF) CRP project 'Self-Powered Body Sensor Network for Disease Management and Prevention Oriented Healthcare' (R-263-000-A27-281).

Reference:

1. S. Suman, M. Gaitan, Y. Joshi, G. G. Harman, *Advanced Packaging, IEEE Transactions on*, **2005**, *28*, 4.
2. C.H. Du, C. Lee, *Jpn. J. Appl. Phys*., **2002**, *41*, 6S.
3. C.H. Du, C. Lee, *Jpn. J. Appl. Phys.*, **2000**, *39*, 12S ,.
4. C. H. Du, C. Lee,. Design, Characterization, and Packaging for MEMS and Microelectronics Bernard Courtois, Serge N. Demidenko Gold Coast, Australia, October, **1999**.
5. H. Zhou, C. Lee, J. Microelectro mech, 2014, (to be published, waiting for DOI number).
6. N.T Nguyen, *Flow Measurement and Instrumentation*, **1997**, *8*, 1
7. C. Hagleitner, A. Hierlemann, D. Lange, A. Kummer, N. Kerness, O. Brand, H. Baltes, *Nature*, **2001**, *414*, 6861.
8. U. A. Dauderstädt, P. H. S. De Vries, R. Hiratsuka, P. M. Sarro, *Sensors and actuators A: Physical*, **1995**,*46*,1.
9. V. Milanović, E. Bowen, M. E. Zaghloul, N. H. Tea, J. S. Suehle, B. Payne, M. Gaitan. *Appl. Phys. Lett.*, **2000**, *76*, 4.
10. M. A. N. F. R. E. D. Klonz, *Instrumentation and Measurement, IEEE Transactions on*, **1987**, *1001,* 2.
11. F. J. DiSalvo, *Science* **1999** , 285, 703 .
12. J. F. Li , W. S. Liu , L. D. Zhao , M. Zhou , *NPG Asia Mater*. **2010**, *2*,152 .
13. M. S. Dresselhaus , G. Chen , M. Y. Tang , R. Yang , H. Lee ,D. Z. Wang , Z. F. Ren , J. P. Fleurial , P. Gogna , *Adv. Mater.* **2007**, *19*, 1043.
14. T. C. Harman , P. J. Taylor , M. P. Walsh , B. E. LaForge , *Science* **2002**, *297*, 2229.
15. G. J. Snyder, E. S. Toberer, *Nat. Mater.* **2008**, *7*, 2.
16. T. M. Tritt, M. A. Subramanian, *Mater. Res. Soc. Symp. Proc.* **2006**, *31*, 03.
17. L. E. Bell, *Science* **2008**, *321*, 5895.
18. J. Xie, C. Lee, M. F. Wang, J. M. Tsai, *Microsyst. Technol.* **2011**, *17*, 1.
19. J. Xie, C. Lee, and H. Feng, *J. Microelectro mech. Syst.* **2010**, *19*, 2.
20. J. Xie, C. Lee, M. F. Wang, Y. Liu and H. Feng, *J. Micromech. Microeng*. **2009**, *19*, 12.
21. W. Glatz, S. Muntwyler, C. Hierold, *Sensors and Actuators A: Physical*, **2006**, *132*, 1.
22. H. Yousef, K. Hjort, and M. Lindeberg, *J. Microelectro mech. Syst.* **2007**, 16, 6.
23. Y. Lan, A. J. Minnich, G. Chen, Z. Ren, *Adv. Fun. Mater.*, **2010**, *20,* 3.
24. Y. Pei, J. Lensch‐Falk, E. S. Toberer, D. L. Medlin, G. J. Snyder, *Adv. Fun. Mater.*, **2011**, *21,* 2.
25. S. N. Girard, , K. Schmidt‐Rohr, , T. C. Chasapis, , E. Hatzikraniotis, , B. Njegic, , E. M. Levin, , A. Rawal, K. M. Paraskevopoulos and M. G. Kanatzidis, *Adv. Fun. Mater.*, **2013**, *23*, 6.
26. L. Hu, T. Zhu, X. Liu, X. Zhao, *Adv. Fun. Mater.*. DOI: 10.1002/adfm.201400474.
27. N. Peranio, E. Leister, W. Töllner, O. Eibl, K. Nielsch, *Adv. Fun. Mater.*, **2012**, *22*, 1.
28. S. Kastbjerg, N. Bindzus, M. Søndergaard, S. Johnsen, N. Lock, M. Christensen, M. Takata, M. A. Spackman, B. B.

Nanoscale Accepted Manuscript

 This journal is © The Royal Society of Chemistry 2012

Iversen, *Adv. Fun. Mater.*, **2013**, *23*, 44.
29. E. S. Toberer, A. Zevalkink, N. Crisosto, G. J. Snyder, *Adv. Fun. Mater.*, 2010, *20*, 24.
30. B. A. Cook, M. J. Kramer, J. L. Harringa, M. K. Han, D. Y. Chung, M. G. Kanatzidis, *Adv. Fun. Mater.*, **2009**, *19*, 8.
31. S. K. Bux, R. G. Blair, P. K. Gogna, H. Lee, G. Chen, M. S. Dresselhaus, R. B. Kaner, J.P. Fleurial, *Adv. Fun. Mater.*, **2009**, *19*, 15.
32. D. L. Medlin, G. J. Snyder, *Current Opinion in Colloid & Interface Science*, **2009**, *14,* 4.
33. C. Dames, G. Chen, in *Thermoelectrics Handbook: Macro to Nano* (ed. Rowe,D. M.) CRC Press, Cleveland **2006**, Ch. 42.
34. Y. S. Ju, K. E. Goodson, *Appl. Phys. Lett.*, **1999**, *74*, 20.
35. A. I. Boukai, Y. Bunimovich, J. Tahir-Kheli, J. K. Yu, W. A. Goddard Iii, J. R. Heath, *Nature* **2008**, *451*, 7175.
36. J. K. Yu, S. Mitrovic, D. Tham, J. Varghese, J. R. Heath, *Nature nanotechnology*, **2010**,*5,* 10.
37. J. Tang, H. T. Wang, D. H. Lee, M. Fardy, Z. Huo, T. P. Russell, P. Yang, *Nano letters*, **2010**,*10*, 10.
38. A. I. Hochbaum, R. Chen, R. D. Delgado, W. Liang, E. C. Garnett, M. Najarian, A. Majumdar, P. Yang, *Nature* **2008**, *451,*7175.
39. D. Li, Y. Wu, P. Kim, L. Shi, P. Yang, A. Majumdar, *Appl. Phys. Lett.* **2003**, *83*, 14.
40. R. Chen, A. I. Hochbaum, P. Murphy, J. Moore, P. Yang, A. Majumdar, *Phys. Rev. Lett.* **2008**, *101,* 10.
41. W. Liu, M. Asheghi, *Journal of heat transfer*, **2006**, *128*, 1.
42. F. Volklein, H. Balles, *J. Microelectro mech. Syst.* **1992**, *1*, 4.
43. O. M. Paul, J. Korvink, and B. Henry, *Sensors and Actuators A: Physical* **1994**, *41*, 1.
44. S. Uma, A. D. McConnell, M. Asheghi, K. Kurabayashi, K. E. Goodson, *International Journal of Thermophysics*, **2001**, *22*, 2.
45. M. M. Mandurah, K. C. Saraswat, C. R. Helms, T. I. Kamins, *J. Appl. Phys.* **1980**, *51*, 11.
46. J. Callaway, *Physic. Rev.* **1959**, *113*, 4.
47. M. G. Holland, *Physic. Rev.*, **1963**, *132*, 6.
48. A. D. McConnell, S. Uma, K. E. Goodson, *J. Microelectro mech. Syst.* **2001**, *10,* 3.
49. H. Zhou, P. Kropelnicki, J. M. Tsai, C. Lee, *J. Micromech. Microeng.* **2013**, *23*, 6.
50. J. Zou, A. Balandin, *J. Appl. Phys.***2001**, *89,* 5.
51. M. Strasser, R. Aigner, C. Lauterbach, T. F. Sturm, M. Franosch, G. Wachutka. *Sensors Actuators A* **2004**, *114*, 2.
52. D. Xu, B. Xiong, and Y. Wang, *J. Microelectro mech. Syst.* **2010**, *19*, 6.
53. L.J. van der Pauw, *Philips Research Reports*, **1958**, *13*, 1.

Nanoscale Accepted Manuscript